Journal of Magnetic Resonance 300 (2019) 135–141

Contents lists available at ScienceDirect

Journal of Magnetic Resonance

journal homepage: www.elsevier.com/locate/jmr

Fibre-orientation dependent $R_1(=1/T_1)$ relaxation in the brain: The role of susceptibility induced spin-lattice relaxation in the myelin water compartment

Felix Schyboll [a], Uwe Jaekel [a], Francesco Petruccione [b], Heiko Neeb [a,c,*]

[a] University of Applied Sciences Koblenz, RheinAhrCampus Remagen, Germany
[b] University of KwaZulu-Natal, Centre for Quantum Technology, Durban, South Africa
[c] Institute for Medical Engineering and Information Processing – MTI Mittelrhein, University of Koblenz, Germany

ARTICLE INFO

Article history:
Received 1 October 2018
Revised 3 January 2019
Accepted 23 January 2019
Available online 25 January 2019

Keywords:
White matter
Fibre orientation
T_1-relaxation
Magnetic susceptibility

ABSTRACT

We have recently observed a dependence of the longitudinal relaxation rate, R_1, on the orientation of nerve fibres with respect to the main magnetic field. A similar dependence of R_2^* is long established and can be well explained by spin-dephasing in an inhomogeneous magnetic field induced by the susceptibility shift between myelin and water protons. The current study investigates if the same effect can also explain the R_1 dependence, neglecting a possible directional dependence of magnetisation transfer between solid myelin and myelin water. A molecular model of the myelin lipid bilayer was employed to simulate the susceptibility induced fields on a microscopic scale for the different nerve fibre orientations. The resulting simulated magnetic fields were used to calculate an orientation dependent relaxation offset, ΔR_1, based on both first-order perturbation theory and a simulation of the spin transition probabilities. Even though both methods yielded consistent orientation dependent relaxation offsets with a distribution that resembles the experimental data, the determined ΔR_1 values are too low to explain the reported R_1 angular dependency. Therefore, unlike R_2^*, susceptibility induced spin flips can be excluded as a dominant source for the observed R_1 angular dependence.

1. Introduction

With the increasing usage of high field systems for research and diagnosis, magnetic susceptibility differences in brain tissue become a more important contrast mechanism in neurological science. For instance, several studies have demonstrated that the R_2^* relaxation rate of the MR signal is influenced by susceptibility differences within nerve bundles and their orientation relative to the main magnetic field [1,2]. Even though a detailed description of this phenomenon is still under progress, the main source has been assigned to an anisotropic susceptibility shift between the myelin sheath and the surrounding tissue [3–5]. It was also shown that the angular dependent contrast provides valuable information about the microstructural compartmentation in white matter (WM) and could serve as diagnostic tool for the investigation of brain degeneration *in vivo* [6].

As we have reported recently, a similar angular dependency can also be observed for the R_1 relaxation rate in WM regions [7]. Specifically, a monotonically increasing R_1 relaxation rate from 1.277 Hz for nerve bundles oriented parallel to 1.311 Hz for nerve bundles oriented perpendicular relative to the B_0-field was observed in healthy subjects investigated at 3 T. The study and understanding of this effect might therefore provide new insights into and a better description of the brain tissue and its microstructure. However, in contrast to R_2^*, the longitudinal relaxation rate is mainly affected by rapidly varying field fluctuations around the Larmor frequency at the site of the hydrogen atoms. This implies that the responsible relaxation mechanism should depend on the fibre orientation, which alters the magnetic field distribution at the site of the proton.

As already suggested in our previous study, susceptibility induced field heterogeneities in the myelin sheath present a potential and obvious source that fulfils both criteria and already serves as basis to explain the R_2^* orientation dependency [8,9]. The basic assumption here is as follows: the susceptibility shift induces local field heterogeneities in the longitudinal (B_z) and transverse (B_x and B_y) directions, dependent on the neuronal fibre orientation relative

---

* Corresponding author at: University of Applied Sciences Koblenz, RheinAhrCampus Remagen, Germany.
E-mail address: neeb@hs-koblenz.de (H. Neeb).

https://doi.org/10.1016/j.jmr.2019.01.013

to the B_0-field. Water molecules diffusing close to the susceptibility source therefore experience temporal varying magnetic fields which depend on the fibre orientation. The resulting field components around the Larmor frequency can in turn increase the transition probability between the spin eigenstates. This effect should be particularly noticeable in the myelin sheath, where the water molecules diffuse predominantly close to the membrane surface and their motility is restricted by the hydrophilic character of phospholipids [10]. These molecules experience the largest field fluctuations with a reduced motility and should therefore predominantly be affected. In contrast, water molecules outside the myelin sheath experience mainly a homogenous magnetic environment and should therefore have an unaffected R_1 relaxation rate.

Therefore, the aim of current work was the investigation of the role of susceptibility induced R_1 relaxation in the myelin water compartment as a function of the fibre orientation relative to the external field. For this purpose, we carried out a molecular dynamic (MD) simulation of a lipid-water system representing a small fraction of the membrane structure inside the myelin sheath. The trajectories of both lipid- and water-associated nuclei obtained from this atomistic simulation were then employed to calculate the time-dependent field at each water-associated hydrogen atom which is induced by point dipoles located at all other nuclei with a strength given by their tissue-specific susceptibility. The whole simulation was repeated for different directions of the membrane structure relative the B_0-field. For each direction, the R_1 relaxation rate was determined using both first-order perturbation theory and the numerically determined spin transition probabilities. The results obtained show that susceptibility induced spin-flips potentially contribute to the effect observed *in vivo*, although with a strength that is four orders of magnitude too small to reproduce the experimental data. These results suggest that other and more dominant relaxation mechanism such as dipole-dipole interaction or magnetization transfer between the myelin membrane and the water compartment might be responsible for the observed angular dependency of R_1.

2. Methods

2.1. Molecular dynamics simulation

To simulate the water dynamics inside the heterogeneous architecture of the myelin sheath, a MD simulation was performed using the GROMACS package 5.1.2 and the GROMOS43a1 coarse-grained force field [11,12]. The membrane structure inside the myelin sheath was modelled by two lipid bilayers containing 200 phospholipids (DPPC) as well as 56 Cholesterol (CHL) lipids, solvated in 7312 SPC/E water molecules [13]. This configuration corresponds to a cholesterol and water concentration of 28% and 43%, respectively, which is in accordance with histological observations [14,15].

Before the production run, during which the nuclear trajectories were sampled, the system was thermodynamically equilibrated for 4 ns to body temperature (310.15 K) and normal pressure. This energy minimisation step is essential to avoid unnecessary distortions of the molecular ensemble when the MD simulation started. The equilibration was performed using the varlet algorithm and a cutoff distance of 12 Å for a Lennard-Jones interaction. For the temperature and pressure coupling, the Berendsen thermostat and barostat with coupling constant of $\tau_T = 0.1$ ps and $\tau_p = 0.5$ps were used, respectively [16]. After the equilibration step, the production run was started from the end-point of the relaxed system and was performed for $T = 12$ ns with a step size of 2 fs at constant energy and volume (NVE-Ensemble). During the production run, the nuclei trajectories of all lipids and the water trapped between the bilayers were saved every 0.5 ps. Both equilibration and production run were performed with periodic boundary condition in all three directions. In order to reduce the influence of discontinuous trajectories from molecules jumping between the aqueous phases at the system boundaries, water molecules outside the bilayer were not considered in the further analysis. This minimises field imperfections and results in a more homogeneous molecular environment for the remaining water molecules. A snapshot of the final bilayer-water configuration after the production run is shown in Fig. 1A.

2.2. Microscopic susceptibility model

The simulation of susceptibility-induced field heterogeneities required the proper definition of a microscopic representation of the magnetic tissue properties. This was realized by employing a non-continuous approach. Specifically, the issue-specific susceptibility was approximated by discrete dipole moments located at the nuclei of the lipid-forming atoms. For simplification and computational efficiency, this model was implemented under the following assumptions: (i) the strength of the magnetic moment is proportional to the nuclear mass (ii) and the spatial location of the dipole is unaffected by light hydrogen atoms. These constraints can be derived from the classical Langevin theory of diamagnetism and, for example, predict the magnetic dipole moment of a water molecule, $\vec{\mu}^{H_20}$, which is, according to the assumptions stated above, spatially located at the oxygen nucleus,

$$\vec{\mu}^{H_20} = \frac{\chi^{H_20}\vec{B}_0}{\mu_0\rho^{H_20}} \tag{1}$$

Here, χ^{H_20} is the magnetic volume susceptibility of water, $\vec{B}_0$ the applied magnetic field, μ_0 the vacuum permeability and ρ^{H_20} the dipole density which in case of water equals the particle density. The expression above can be easily derived from the macroscopic definition of magnetization and holds true for simple molecular structures with isotropic susceptibility. In order to model the field distortions induced by more complex lipid molecules with anisotropic susceptibility, Eq. (1) was transformed to the laboratory frame shown in Fig. 1B and weighted by the nuclei mass of each constituent of the complex molecule. The dipole moment of a single nucleus, *n*, inside the macromolecule can then be written as (see Appendix A)

$$\vec{\mu}_n^{lipid}(\theta,\varphi) = \kappa_n^{lipid}\frac{\vec{B}_0}{\mu_0\rho_n^{lipid}}\left(\chi_\perp + \left(\chi_\parallel - \chi_\perp\right)\cos(\theta)^2\sin(\varphi)^2\right) \tag{2}$$

where θ and φ describe the fibre orientation relative to the $\vec{B}_0$-field and the position of the macromolecule inside the cylindrical myelin sheath, respectively, ρ_n^{lipid} the nuclear density and κ_n^{lipid} the mass fraction of the *n*-th constituent of the corresponding DPPC or CHL lipid. The terms $\chi_\parallel$ and $\chi_\perp$ arise from the anisotropic molecular structure and represent the volume susceptibility of lipids orientated parallel and perpendicular to the B_0-field, respectively. To satisfy the assumptions stated above, Eq. (2) was applied to each non-hydrogen nuclei of a macromolecule and the dipole moments were localized according to the mass fraction κ at the corresponding nuclei positions. This spatial distribution implies, apart from a slight shift due to ignoring the hydrogen atoms, that the magnetic centre of each lipid is located in its centre-of-mass, in accordance with the Langevin theory of diamagnetism.

Here, it should be noted that the presented model does not account for the effect that is described by the Lorentz correction in continuous approaches to simulate the spin coherence loss caused by the average field heterogeneities in z-direction. The Lor-

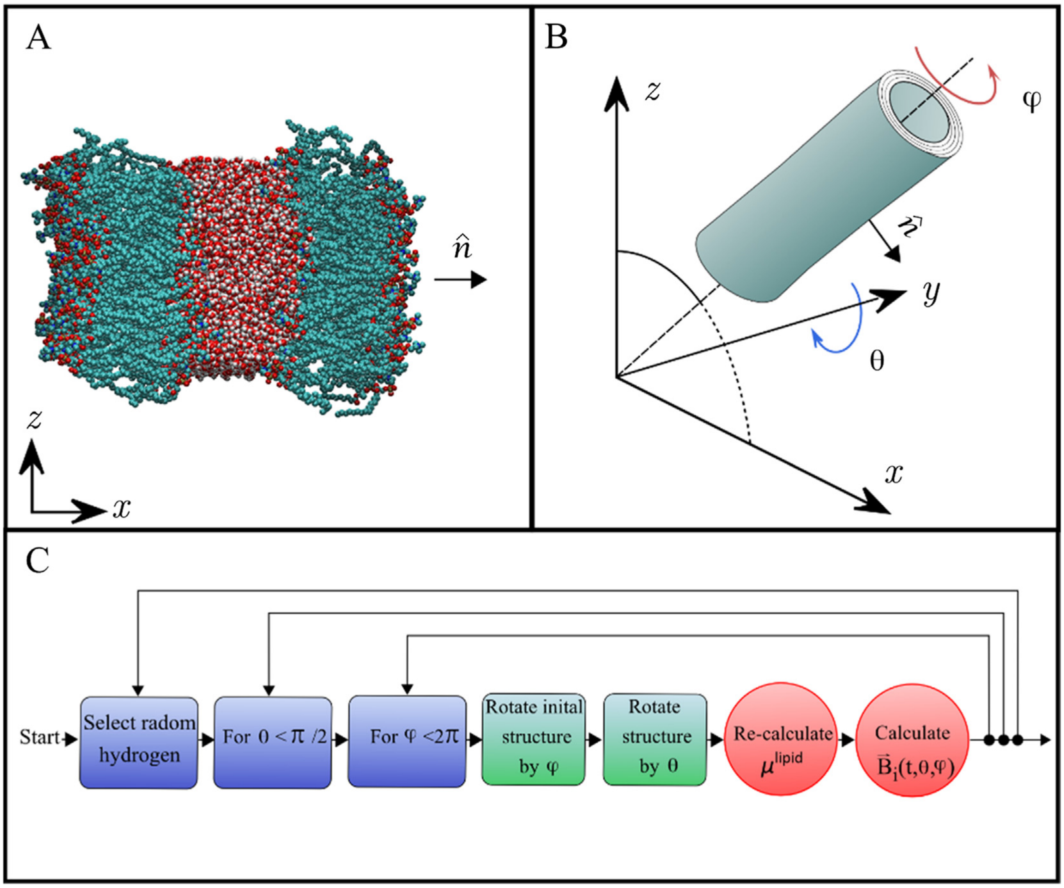

Fig. 1. Snapshot of the bilayer-water system after the production run without the outer water molecules (A); a schematic illustration of the laboratory frame coordinate system (B) and a flowchart of the rotation procedure described in the method section (C).

entz correction is required as the near field induced by an ensemble of dipoles in the immediate environment of randomly diffusing water molecules cancels out. This contribution has therefore to be subtracted from the macroscopic field to obtain the absolute field in the z-direction experienced by a proton. However, the current work did not focus on the spin coherence loss caused by the macroscopic field heterogeneities in the z-direction responsible for T_2^* relaxation, but instead investigated the influence of local field fluctuations in the x- and y-directions that potentially increase the R_1-relaxation rate. This also implies that the total susceptibility and not just the susceptibility shifts relative to the surrounding tissue is of importance, as this determines the total field in x- and y-direction experienced by diffusing protons. Therefore, the strength of the dipole moments was calculated using $\chi^{H_20} = -9.035$ ppm for water as well as $\chi_{\parallel} = -10.43$ ppm and $\chi_{\perp} = -9.30$ ppm for the lipids, where it was assumed that the diamagnetic properties of CHL and DPPC lipids are comparable and can therefore be expressed by same susceptibility [17]. Using these parameters and Eq. (1), the magnetic dipole moment of water molecules is $\vec{\mu}^{H_20} = -5.03 \times 10^{-28}$ Am^2 at 3 T. The remaining parameters κ_n^{lipid} and ρ_n^{lipid} for the determination of $\vec{\mu}_{lipid}$ were extracted from the MD simulation and calculated using the reported lipid volumes of $V^{DPPC} = 1232$ Å^3 and $V^{CHL} = 630$ Å^3 [18]. As such, the particle density ρ_c^{CHL} of the carbon atoms inside the CHL($C_{27}H_{46}O$) lipids is then simply given by $\rho_c^{CHL} = 27/V^{CHL}$. Using this value with the corresponding mass fraction of $\kappa_c^{lipid} = 3.5\%$, Eq. (2) results in a magnetic dipole strength of μ_c^{CHL} in the range between -2.05×10^{-28}Am^2 to -1.83×10^{-28} Am^2 at 3 T, depending on the angles θ and φ. In the same way, the magnetic moments of the other non-hydrogen atoms inside CHL and DDPC($C_{40}H_{80}NO_8P$) were calculated and assigned to the corresponding atom.

2.3. Microscopic field simulation

Based on the trajectories extracted from the MD simulation, the orientation- and time-dependent field perturbations were simulated as follows: First, the susceptibility-specific dipole moments were assigned to the non-hydrogen atoms using the microscopic susceptibility model described above for an external field of 3 T aligned along the z-axis. Second, the whole trajectory set was successively rotated in 15 steps counter clockwise by an angle φ around the z-axis, in order to sample different position around the axon. For each rotation angle φ, the dipole moments assigned to the lipid molecules were re-calculated according to Eq. (2) and the effective field at a randomly selected hydrogen atom,i, located on the j-th water molecule was determined by

$$\vec{B}_i(\theta,\varphi,t) = \frac{\mu_0}{4\pi}\sum_{k\neq j}^{N}\frac{3\vec{r}_{ki}\left(\vec{\mu}_k(\theta,\varphi)\cdot\vec{r}_{ki}\right) - \vec{\mu}_k(\theta,\varphi)r_{ki}^2}{r_{ki}^5}, \tag{3}$$

where N is the total number of simulated dipoles (located on both lipids and water molecules), $\vec{\mu}_k$ is the magnetic moment of the k-th dipole as given by Eq. (2), $\vec{r}_{ki} = f(\theta,\varphi,t)$ the corresponding distance vector between the i-th water proton and the k-th magnetic dipole and t the simulation time. Here, the case $k = j$ describes the intramolecular interaction between the proton spin and the surrounding electron cloud and is responsible for the so-called nuclear shielding effect causing a spectral peak shifting and line broadening. Since this effect is assumed to be orientation independent for fast tumbling molecules such as water and requires a more complex treatment, the intramolecular interaction was not considered in Eq. (3) [19].

In order to simulate the field fluctuations for different fibre orientations, the fibre axis was tilted in steps of 6° around the y-axis and the whole procedure was repeated as described above. This step was performed 15 times, resulting in a maximum angle $\theta_{max} = 90^\circ$ that corresponds to a perpendicular fibre orientation towards to B_0-field. A schematic illustration of the described procedure is shown in Fig. 1C. Finally, to obtain only the fluctuating component of the magnetic field, $\vec{B}^{Fl.}$, the time independent field offset was subtracted,

$$\vec{B}^{Fl.}(t,\theta,\varphi) = \vec{B}(t,\theta,\varphi) - \overline{\vec{B}(t,\theta,\varphi)} \tag{4}$$

The bar over the second term on the right-hand site denotes the time average. The whole procedure was repeated for 1828 randomly selected water protons and yields the time and angular dependent magnetic fields for 225 different combinations of θ and φ for each proton. The resulting dataset consisting of 411,300 simulated time dependent magnetic fields, $\vec{B}^{Fl.}(t,\theta,\varphi,i)$, forms the basis for the calculation of the orientation dependent R_1 relaxation rate as described in the following. The index$i = 1, \ldots, 1828$ labels each individual proton sampled.

2.4. Computation of the R_1-relaxation rate

Based on the time dependent magnetic fields, $\vec{B}^{Fl.}(t,\theta,\varphi,i)$, the R_1 rates were determined employing two different approaches. First, the decay rates were calculated using the standard textbook formulas which are based on first order perturbation theory [20]. This commonly employed approach decouples the magnitude of the matrix elements from the spectral density, and thus allows for the separate evaluation of their respective contribution to the R_1 angular dependence. Second, the transition rates were calculated from the magnetic field dependent time-evolution of spin eigenstates by numerically solving the time dependent Schrödinger equation. Even though this approach is computationally more demanding, it is not restricted to the first order truncation of the quantum mechanical time evolution operator and as such potentially less biased, at least for short simulation times.

For calculating the decay rate using first-order perturbation theory, we followed the convention by McConell but adapting this approach for a heterogeneous environment by assuming anisotropic field fluctuations ($B_x^{Fl.} \neq B_y^{Fl.}$) with uncorrelated and exponentially decaying spectral densities [20]. The relaxation rate can then be written as

$$R_1(\theta,\varphi) = \gamma^2\left(\overline{B_x^{Fl.}(\theta,\varphi)^2}\,\tau_x(\theta,\varphi) + \overline{B_y^{Fl.}(\theta,\varphi)^2}\,\tau_y(\theta,\varphi)\right), \tag{5}$$

where γ is the gyromagnetic ratio of the protons and $\tau_x(\tau_y)$ is the corresponding correlation time for the time dependent field fluctuations in the *x*- or *y*-direction. The overbar denotes the average over time, T, and over the different protons sampled (index i). For simplicity, we assumed $B_0\gamma\tau_x(\tau_y) \ll 1$ in Eq. (5) which is reasonable for rapidly tumbling molecules at conventional field strength. The correlation times describe the decay of the spectral density and were calculated from the autocorrelation function (ACF) which is given by

$$G_\alpha(\tau,\theta,\varphi) = \overline{B_\alpha^{Fl.}(t+\tau,\theta,\varphi)B_\alpha^{Fl.}(t,\theta,\varphi)} = \overline{B_\alpha^{Fl.}(\theta,\varphi)^2}\,e^{-\frac{|\tau_\alpha(\theta,\varphi)|}{\tau}}, \tag{6}$$

where τ is the lag time and the subscript α indexes the direction (x or y) of the corresponding field fluctuation. Again, the overbar represents both time and sample average. The ACF was computed based on the simulated time dependent magnetic fields at different lag times, $0<\tau<250$ ps, using fast Fourier transformation and was subsequently normalized by $G_\alpha(\tau,\theta,\varphi)/G_\alpha(0,\theta,\varphi)$. For a precise and accurate quantification of $\tau_\alpha(\theta,\varphi)$, it must be considered that the tail of the ACF decays slowly and is not necessarily exponential over the full range [21]. Therefore, the ACF was divided into two parts at a cutoff value of $\tau = 5$ ps. The correlation time was then determined using explicit integration of the first and analytical integration of the second part (the tail), after fitting it to the exponential term in Eq. (6) as described in [22]. Different values for the maximum lag time ([100, 400, 600 ps]) and the cutoff time ([3, 8, 10 ps]) yielded comparable R_1 rates with similar orientation dependencies.

To ensure that the results obtained are not due to potential systematic errors caused by neglecting higher order terms in the perturbation expansion, the relaxation rates were also calculated from the transition probabilities given by the solution of the time-dependent Schrödinger equation,

$$\begin{aligned} i\hbar\frac{d}{dt}|\psi_k(t)\rangle &= (H_0 + H_1(t,k))|\psi_k(t)\rangle \\ &= -\gamma(B_0\sigma_z + B_x^{Fl.}(t,k)\sigma_x + B_y^{Fl.}(t,k)\sigma_y \\ &\quad + B_z^{Fl.}(t,k)\sigma_z)|\psi_k(t)\rangle \end{aligned} \tag{7}$$

Here, $\hbar$ is the reduced Planck constant,$|\psi_k(t)\rangle$ the spin state of the k-th proton, H_0 and $H_1(t)$ the time dependent and independent Hamiltonians, respectively, and σ are the Pauli matrices. We assumed that the time independent field offset eliminated in Eq. (4) is negligible and does not substantially affect the results, which is justified as $\left|\overline{\vec{B}(t,\theta,\varphi)}\right| \ll B_0$. To evolve the spin system, the initial state $|\psi(0)\rangle$ was set to the ground state antiparallel to the B_0-field ('spin-down') and Eq. (7) was solved in the interaction picture using a 4th order Runge-Kutta method. For an isolated spin system with two energy eigenstates, the R_1 relaxation rate is then given by the transition probability from spin-state $|\psi_k(T)\rangle$ at time T to the final spin-up state, $|\psi_\beta\rangle$, averaged over all states k and normalised by T. It can thus be written as

$$R_1(\theta,\varphi) = \frac{1}{NT}\sum_{k=1}^{N}|\langle\psi_\beta|\psi_k(T,\theta,\varphi)\rangle|^2 = \frac{1}{NT}\sum_{k=1}^{N}|\langle\psi_\beta|U_k(\theta,\varphi,t)|\psi(0)\rangle|^2 \tag{8}$$

where $|\psi_k(T,\theta,\varphi)\rangle$ is the spin-state of the k-th proton after the simulation time T, $U_k(\theta,\varphi,t)$ is the associated time evolution operator in the interaction picture, $|\psi_\beta\rangle$ is the final spin up-state and $N = 1828$ the total number of simulated protons. The right-hand side of Eq. (8) denotes the transition probability for a spin flip divided by the simulation time, which is constant for weak perturbations as long as $T \ll T_1$ is satisfied (Fermi's golden rule).

The R_1 relaxation rates obtained with both approaches were finally averaged over the segment positions (angle φ), yielding the effective R_1 angular dependent relaxation rate, $R_1(\theta)$, that would be measured in an NMR experiment.

3. Results

Fig. 2A shows the R_1 relaxation rates calculated from Eq. (8) as a function of the fibre orientation (θ) and membrane positions (φ) within the myelin sheath. Up to angle of $\theta = 20^\circ$, $R_1 \approx 150$ μHz is almost constant. At angles $\theta > 20^\circ$, the relaxation rate begins to oscillate periodically between 90 and 220 μHz as a function of both θ and φ. Similar results with an identical pattern were also

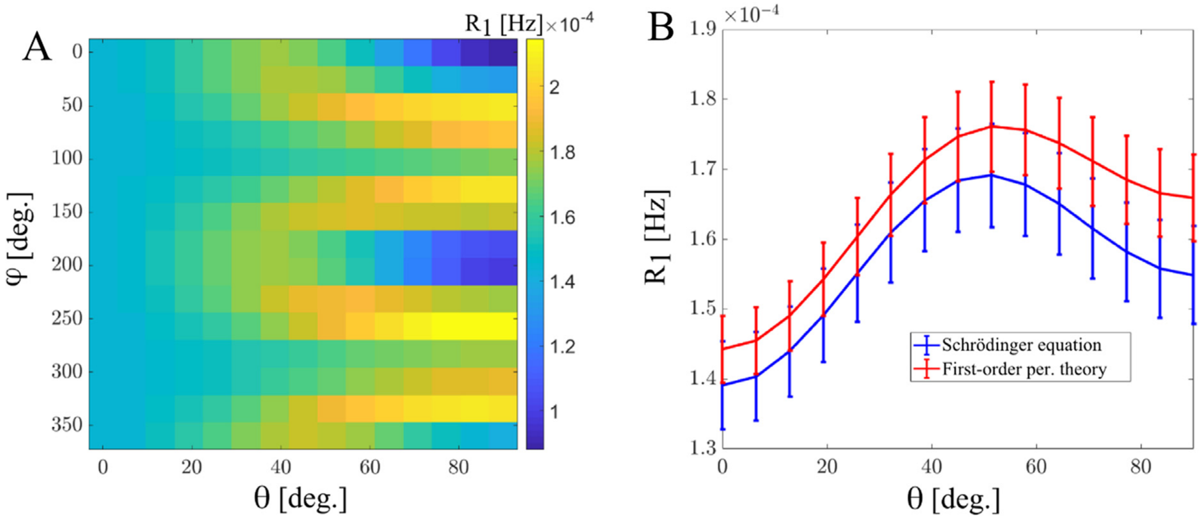

Fig. 2. R1 relaxation rate as a function of the fibre orientation (θ) and segment positions (φ) within the sheath calculated by first order perturbation theory (A). R1 relaxation averaged over φ as a function of fibre direction calculated from Eqs. (8) and (5), respectively. The error bars indicate the standard error of mean.

obtained for the R$_1$ rates calculated within the framework of first order perturbation theory (Eq. (8)). Fig. 2B shows the R$_1$ rates calculated with Eq. (8) as well as Eq. (5) and averaged over the segment positions (φ). As it is evident from this figure, both methods predict an angular dependent longitudinal relaxation rate with an almost identical distribution, apart from a constant offset of approximate 10 μHz. The averaged relaxation rates calculated with first-order perturbation theory increases from 144 μHz by 32 μHz in the intervals [0–50°] and decreases for $\theta > 50°$ by 10μHz. In contrast, the average R$_1$ rate determined with Eq. (8) increases from 134 by 30 μHz and decreases slightly more by 14 μHz at angles $\theta > 50$. Using these data, the orientation dependent relaxation offset, $\Delta R_1 = R_1(90°) - R_1(0°)$, was 22 μHz for the first and 16 μHz for the second method.

Fig. 3 shows the mean square magnitude, $B_\alpha^{Fl.}(\theta)^2$, of the angular dependent magnetic field fluctuations in the x- and y-direction, respectively, as well as the corresponding correlation times averaged over the segment positions (angle φ). For a better comparability and to assess the influence of the individual parameters on R$_1$, all four curves were normalized relative to their initial values of $B_\alpha^{Fl.}(0)^2 = 55$ nT^2 and $\tau_\alpha(0) = 16$ ns. As evident from Fig. 3, the normalized correlation times τ_α increase by approx. 65 (50) % and reach their maximum at 45 (90) degrees, respectively. Here, it is remarkable that the average of both correlation times clearly reflects the R$_1$ behaviour shown in Fig. 2. In contrast, the normalized field fluctuation show no significant angular dependency with small variations between 2% and −3%.

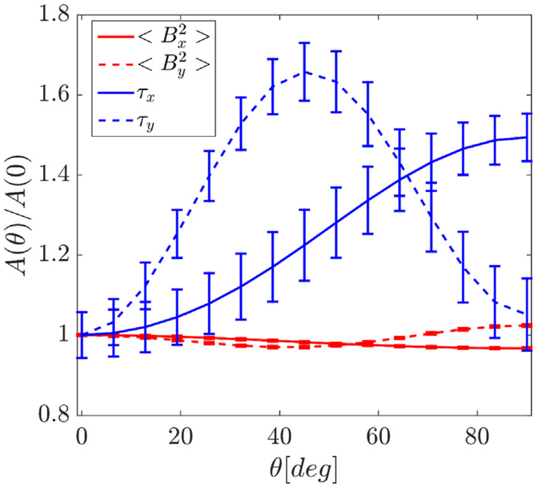

Fig. 3. Normalized correlation times and mean square of the magnetic field strength averaged over φ and as a function of fibre direction. The error bars indicate the standard error of mean.

4. Discussion

In this study we investigated the influence of susceptibility induced R$_1$ relaxation in myelin water and its orientation dependency relative to the main magnetic field. The results obtained clearly demonstrate that the induced field heterogeneities affect R$_1$ and increases the relaxation rate with increasing angle. Moreover, the good comparability between the R$_1$ distributions in Fig. 2B shows that both methods employed for the calculation of relaxation rates are sensitive to small variations of the magnetic environment and yield consistent results, apart from a constant offset. As it is obvious from Fig. 3, the main contribution to the R$_1$ behavior can indeed be attributed to the angular dependent correlation times. Here, the positions of the maxima and the functional behaviour strongly suggest that the simulated R$_1$ rates can be approximated by a linear combination of a $\sin(\theta)^2$ and a $\sin(2\theta)^2$ term. In contrast, the relative changes of the average field fluctuations are significant smaller and show only a negligible effect on the angular dependence of R$_1$.

When comparing the simulated results with the experimental findings from the previous study, it must be considered that the *in vivo* measurements reflect the average R$_1$ rate across a single voxel containing distinct water compartments (or pools). In WM regions, these compartments are in mutual exchange with each other and can be categorized according to their specific relaxation rates in a myelin water and a free water pool, whereby the latter summarizing all compartments with unrestricted molecular motility (axonal and interstitial water) [23,24]. If one assumes that the magnetization exchange between the pools is fast compared to the T$_1$ relaxation time of the myelin pool, the experimentally determined R$_1$ rate is simply the sum of the compartment specific R$_1$ weighted by their respective pool fraction [25,26]. Using this assumption of fast exchange, the orientation dependent relaxation offset in the myelin pool can be written as

$$\Delta R_1^{app.} = R_1^{app.}(90^\circ) - R_1^{app.}(0^\circ) = \alpha(R_1^{my.}(90^\circ) - R_1^{my.}(0^\circ)) \tag{9}$$

where $R_1^{app.}$ is the experimental observed R_1 rate, α the MR-visible water fraction of the myelin pool and $R_1^{my.}$ the corresponding relaxation rate. Using the reported values for $R_1^{exp.}$ (see Section 1) and a typical myelin water fraction of approximate 10% of the total MR-visible water content, the experimentally observed $\Delta R_1^{my.}$ is in the order of 0.34 Hz [27]. A similar result would be obtained using a slow exchange model instead of the fast exchange model employed here [23]. Assuming a cross relaxation rate of 10 Hz between the compartments and R_1 relaxation rates of 1.2 Hz and 2.5 Hz for the free water and the myelin water pool [28,29], respectively, results in a minor change of $\Delta R_1^{my.}$ from 0.34 Hz to 0.42 Hz.

Both results are four orders of magnitude larger than the value calculated in the current study (ΔR_1 of 16 μHz to 22 μHz). In order to reconstruct the experimental data, the field fluctuation would have to be a factor 100 larger or the correlation times have to be in the order of a several hundred microseconds. This discrepancy is too large to be explainable by simulation-related or numerical errors and excludes the susceptibility induced field heterogeneities as the main source of the experimentally determined R_1 angular dependency. Furthermore, the simulated results also demonstrate that diamagnetic differences between water and tissue have a negligible effect on the apparent R_1 rate at conventional field strength, even in a unique environment such as the myelin sheath. This conclusion should also hold true for higher field strengths, even considering the quadratic dependence of R_1 on the induced magnetic field and therefore B_0 (see Eqs. (5), (3) and (1)). Assuming that the simulated results can be extrapolated to higher values of B_0, the R_1 relaxation would be given by $R_1(B_0) \approx \frac{1.44\mu Hz}{9T^2} B_0^2$. This implies that even at field strengths as high as 50 T, the susceptibility induced R_1 relaxation is in the order of a few mHz and thus still negligible compared to the total relaxation rate. Therefore, the observed dispersion relation, $T_1 = T_1(\omega)$ (see e.g. [30]), is influenced by effects different from longitudinal relaxation in the field induced by an inhomogeneous diamagnetic microstructure.

Even though a more realistic model of the myelin architecture by including other lipids/proteins or a more precise modeling of the susceptibility with a different weighting of the spatial distribution of the discrete magnetic dipoles would affects the results, this should not significantly change the final interpretation.

Therefore, the question what causes the angular dependent R_1 relaxation and which physical or physiological effects may play a potential role is still open. A possible hint to resolve this issue might be provided by the correlation times shown in Fig. 3. Here, it is notable that τ_α increases by about 50 percent and mainly defines the shape of the R_1 curve. In turn, this means that the half-width of the intermolecular spectral density is strongly affected by the fibre orientation. The most likely reason for this line broadening could be (i) the pronounced short-range order in the myelin sheath and/or (ii) the anisotropic diffusion coefficient of the water molecules at the membrane surface due to the lipid hydrophilicity [31,32]. Both aspects could also affect the spectral density of other coupling mechanism such as inter- and intramolecular spin-spin interaction and thus contribute to the observed angular dependent R_1 rate. The influence of an orientation dependent spin-spin interaction on $R_1(\theta)$ can be easily demonstrated using Eq. (9). Assuming that the main part of $R_1^{my.} = 1.2 - 20\text{Hz}$ [33,34] is due to dipole-dipole interactions and that the corresponding correlation time increases with increasing angle by approx. 10 percent, Eq. (9) yields $\Delta R_1^{app.} = 0.034$ Hz, consistent with experimental results. Of course, it has to be considered that other relaxation mechanisms such as chemical exchange between the myelin membrane and the surrounding water strongly contribute to $R_1^{my.}$, which are, however, probably orientation independent. On the other side, the cross relaxation between the pools is dominated by the dipole-dipole interaction and could thus contribute to the observed effect.

Moreover, it should also be noted, that we modelled the diamagnetic susceptibility with purely polarized dipole moments aligned along the z-axis. In contrast, the dipole-dipole relaxation is caused by the nuclei spin with polarization given by the Boltzmann-distribution. This weaker polarization may result in a reduced change of the spectral density and therefore a decreased $\Delta R_1^{my.}$.

Nonetheless, the simulated results clearly suggest that the correlation between $\tau_\alpha(\theta)$ and θ is positive rather than negative and that the T_1(=1/R_1) time reaches its minimum at approx. 50°. This outcome is in disagreement with the experimental results recently published by Knight et al. [35]. These authors reported an increasing T_1 time (decreasing R_1 rate) up to approx. θ = 50–60° followed by a strong decrease, which is in contradiction to both simulated $\tau_\alpha(\theta)$ and experimental data reported in our previous study [7]. However, a detailed discussion of potential reasons for these discrepancies including i.e. a more detailed investigation of the influence of dipole-dipole interaction and the influence of magnetization transfer effects is outside the scope of the current work but could be an interesting issue of future studies.

5. Conclusion

In conclusion, the current study shows that even though the susceptibility induced R_1 relaxation in myelin water depends on fibre orientation, the effect is too small to be responsible for the experimentally reported R_1 angular dependency. Here, it is remarkable that $R_1(\theta)$ is mainly defined by the correlation time instead of the strength of the fluctuating magnetic field. This fact suggests that other relaxation mechanisms such as the inter- and intramolecular dipole-dipole relaxation, which are strongly affected by the molecular dynamics and environment, could be potential sources for explaining the angular dependency of R_1.

Acknowledgements

The authors wish to thank Jens Nettersheim for his support with the GROMACS software package and useful discussions on the development and implementation of the field simulation.

Appendix A. Derivation of the magnetic moment induced by an anisotropic susceptibility.

To extend Eq. (1) to systems with anisotropic magnetic susceptibility such as lipids, we used the convention $\chi_a = \chi_\parallel - \chi_\perp$ for the anisotropic shift and defined the hydrocarbon chain of the lipid as main axis. The susceptibility can then be written as a function of the lipid orientation in the main magnetic field and is given by

$$\begin{aligned}\vec{\mu}(\gamma) &= \frac{\vec{B}_0}{\mu_0\rho}\chi(\gamma) = \frac{\vec{B}_0}{\mu_0\rho}\left[\chi_\parallel \cos(\gamma)^2 + \chi_\perp \sin(\gamma)^2\right] \\ &= \frac{\vec{B}_0}{\mu_0\rho}\left[\chi_\perp \cos(\gamma)^2 + \chi_{a.}\cos(\gamma)^2 + \chi_\perp \sin(\gamma)^2\right] \\ &= \frac{\vec{B}_0}{\mu_0\rho}\left[\chi_\perp + \chi_{a.}\left(\frac{\hat{n}\cdot\vec{B}_0}{\left|\vec{B}_0\right|}\right)^2\right],\end{aligned} \tag{A1}$$

where γ is the angle between the normal vector$\hat{n}$ of the membrane surface and the $\vec{B}_0$–field, which corresponds to the main axis of the hydrocarbon chain. Transforming this expression into the frame of reference shown in Fig. 1B, and applying the corresponding rotation matrix to tilt the nerve fibre around the y-axis, the normal vector can be written as

$$\hat{n} = R_y \cdot \begin{pmatrix} \cos(\varphi) \\ \sin(\varphi) \\ 0 \end{pmatrix} = \begin{pmatrix} \cos(\theta)\cos(\varphi) \\ \sin(\varphi) \\ -\sin(\theta)\cos(\varphi) \end{pmatrix}, \tag{A2}$$

where R_y is the rotation matrix,φ the azimuth and θ the elevation angle describing the lipid position inside the myelin sheath and the fibre direction towards the $\overrightarrow{B}_0$ -field, respectively. Inserting this expression into (A1), the magnetic dipole moment can be rewritten as

$$\begin{aligned} \overrightarrow{\mu}(\theta,\varphi) &= \frac{\overrightarrow{B}_0}{\mu_0\rho}\left[\chi_\perp + \chi_{a.}\left(\frac{\hat{n}\cdot\overrightarrow{B}_0}{\left|\overrightarrow{B}_0\right|}\right)^2\right] \\ &= \frac{\overrightarrow{B}_0}{\mu_0\rho}\left[\chi_\perp + \chi_{a.}\left(\frac{-\sin(\theta)\cos(\varphi)}{\sqrt{\hat{n}}}\right)^2\right] \\ &= \frac{\overrightarrow{B}_0}{\mu_0\rho}\left[\chi_\perp + \left(\chi_\parallel - \chi_\perp\right)\sin(\theta)^2\cos(\varphi)^2\right]. \end{aligned} \tag{A3}$$

Here, it should be noted that the final expression holds only true for a fixed $\overrightarrow{B}_0$-field along the z-axis and a fibre rotation around the y-axis.

References:

[1] B. Bender, U. Klose, The in vivo influence of white matter fiber orientation towards B0 on T2* in the human brain, NMR Biomed. 23 (9) (2010) 1071–1076.

[2] C. Denk, E.H. Torres, A. MacKay, A. Rauscher, The influence of white matter fibre orientation on MR signal phase and decay, NMR Biomed. 24 (3) (2011) 246–252.

[3] J. Lee, K. Shmueli, B.-T. Kang, B. Yao, M. Fukunaga, P. Van Gelderen, S. Palumbo, F. Bosetti, A.C. Silva, J.H. Duyn, The contribution of myelin to magnetic susceptibility-weighted contrasts in high-field MRI of the brain, Neuroimage 59 (4) (2012) 3967–3975.

[4] S.-H. Oh, Y.-B. Kim, Z.-H. Cho, J. Lee, Origin of B0 orientation dependent R2*(= 1/T2*) in white matter, Neuroimage 73 (2013) 71–79.

[5] P. Sati, A.C. Silva, P. van Gelderen, M.I. Gaitan, J.E. Wohler, S. Jacobson, J.H. Duyn, D.S. Reich, In vivo quantification of T2* anisotropy in white matter fibers in marmoset monkeys, Neuroimage 59 (2) (2012) 979–985.

[6] E. Hernández-Torres, V. Wiggermann, S. Hametner, T.R. Baumeister, A.D. Sadovnick, Y. Zhao, L. Machan, D.K. Li, A. Traboulsee, A. Rauscher, Orientation dependent MR signal decay differentiates between people with MS, their asymptomatic siblings and unrelated healthy controls, PLoS ONE 10 (10) (2015) e0140956.

[7] F. Schyboll, U. Jaekel, B. Weber, H. Neeb, The impact of fibre orientation on T 1-relaxation and apparent tissue water content in white matter., Magn. Reson. Mater. Phys., Biol. Med. (2018) 1–10.

[8] P. Sati, P. van Gelderen, A.C. Silva, D.S. Reich, H. Merkle, J.A. De Zwart, J.H. Duyn, Micro-compartment specific T2* relaxation in the brain, Neuroimage 77 (2013) 268–278.

[9] S. Wharton, R. Bowtell, Fiber orientation-dependent white matter contrast in gradient echo MRI, Proc. Natl. Acad. Sci. (2012), 201211075.

[10] R. Peters, K. Beck, Translational diffusion in phospholipid monolayers measured by fluorescence microphotolysis, Proc. Natl. Acad. Sci. 80 (23) (1983) 7183–7187.

[11] B. Hess, C. Kutzner, D. Van Der Spoel, E. Lindahl, GROMACS 4: algorithms for highly efficient, load-balanced, and scalable molecular simulation, J. Chem. Theory Comput. 4 (3) (2008) 435–447.

[12] W.F. van Gunsteren, H.J. Berendsen, Groningen molecular simulation (GROMOS) library manual, Biomos, Groningen 24 (682704) (1987) 13.

[13] O. Berger, O. Edholm, F. Jähnig, Molecular dynamics simulations of a fluid bilayer of dipalmitoylphosphatidylcholine at full hydration, constant pressure, and constant temperature, Biophys. J . 72 (5) (1997) 2002–2013.

[14] S. Shah, N. Peterson, C. McKean, Lipid composition of human cerebral white matter and myelin in phenylketonuria 1, J. Neurochem. 19 (10) (1972) 2369–2376.

[15] G.J. Siegel, Basic neurochemistry: molecular, cellular and medical aspects. vol V360 SIEb, 1999.

[16] H.J. Berendsen, J.v. Postma, W.F. van Gunsteren, A. DiNola, J. Haak, Molecular dynamics with coupling to an external bath, J. Chem. Phys. 81 (8) (1984) 3684–3690.

[17] C. Liu, W. Li, K.A. Tong, K.W. Yeom, S. Kuzminski, Susceptibility-weighted imaging and quantitative susceptibility mapping in the brain, J. Magn. Reson. Imaging 42 (1) (2015) 23–41.

[18] A.I. Greenwood, S. Tristram-Nagle, J.F. Nagle, Partial molecular volumes of lipids and cholesterol, Chem. Phys. Lipids 143 (1) (2006) 1–10.

[19] K. Modig, B. Halle, Proton magnetic shielding tensor in liquid water, J. Am. Chem. Soc. 124 (40) (2002) 12031–12041.

[20] A. Carrington, A.D. McLachlan, Introduction to magnetic resonance: with applications to chemistry and chemical physics, 1967.

[21] M. Allen, D. Tildesley, Computer Simulation of Fluids., Oxford Science Publications, 1987.

[22] D. van der Spoel, P.J. van Maaren, H.J. Berendsen, A systematic study of water models for molecular simulation: derivation of water models optimized for use with a reaction field, J. Chem. Phys. 108 (24) (1998) 10220–10230.

[23] J.G. Sled, G.B. Pike, Quantitative imaging of magnetization transfer exchange and relaxation properties in vivo using MRI, Magn. Reson. Med.: Off. J. Int. Soc. Magn. Reson. Med. 46 (5) (2001) 923–931.

[24] G.B. Pike, Pulsed magnetization transfer contrast in gradient echo imaging: a two-pool analytic description of signal response, Magn. Reson. Med. 36 (1) (1996) 95–103.

[25] J. Zimmerman, W.E. Brittin, Nuclear magnetic resonance studies in multiple phase systems: lifetime of a water molecule in an adsorbing phase on silica gel, J. Phys. Chem. 61 (10) (1957) 1328–1333.

[26] G.D. Fullerton, J.L. Potter, N.C. Dornbluth, NMR relaxation of protons in tissues and other macromolecular water solutions, Magn. Reson. Imaging 1 (4) (1982) 209–226.

[27] A. Mackay, K. Whittall, J. Adler, D. Li, D. Paty, D. Graeb, In vivo visualization of myelin water in brain by magnetic resonance, Magn. Reson. Med. 31 (6) (1994) 673–677.

[28] G.J. Stanisz, A. Kecojevic, M. Bronskill, R. Henkelman, Characterizing white matter with magnetization transfer and T2, Magn. Reson. Med.: Off. J. Int. Soc. Magn. Reson. Med. 42 (6) (1999) 1128–1136.

[29] C. Lenz, M. Klarhöfer, K. Scheffler, Limitations of rapid myelin water quantification using 3D bSSFP, Magn. Reson. Mater. Phys., Biol. Med. 23 (3) (2010) 139–151.

[30] W.D. Rooney, G. Johnson, X. Li, E.R. Cohen, S.G. Kim, K. Ugurbil, C.S. Springer Jr, Magnetic field and tissue dependencies of human brain longitudinal 1H2O relaxation in vivo, Magn. Reson. Med.: Off. J. Int. Soc. Magn. Reson. Med. 57 (2) (2007) 308–318.

[31] J.-L. Rigaud, C. Gary-Bobo, Y. Lange, Diffusion processes in lipid-water lamellar phases., Biochimica et Biophysica Acta (BBA)-Biomembranes 266 (1) (1972) 72–84.

[32] G.J. Tiddy, Surfactant-water liquid crystal phases, Phys. Rep. 57 (1) (1980) 1–46.

[33] J.L. Lancaster, T. Andrews, L.J. Hardies, S. Dodd, P.T. Fox, Three-pool model of white matter, J. Magn. Reson. Imaging 17 (1) (2003) 1–10.

[34] J.A. Rioux, I.R. Levesque, B.K. Rutt, Biexponential longitudinal relaxation in white matter: characterization and impact on T1 mapping with IR-FSE and MP2RAGE, Magn. Reson. Med. 75 (6) (2016) 2265–2277.

[35] M.J. Knight, R.A. Damion, R.A. Kauppinen, Observation of angular dependence of T1 in the human white matter at 3T, Biomed. Spectrosc. Imaging 7 (3–4) (2018) 125–133.